IEEE Access
Multidisciplinary | Rapid Review | Open Access Journal

Date of publication xxxx 00, 0000, date of current version xxxx 00, 0000.

Digital Object Identifier 10.1109/ACCESS.2022.Doi Number

Analysis of Near-Field EM Energy Densities for UCA-OAM Wave Based on Infinitesimal Dipoles

Jaehoon Jeong[1] and Young-Dam Kim[2]

[1]Korea Aerospace Research Institute, Daejeon 34133, Republic of Korea
[2]Department of Electronics Engineering, Chungnam National University, Daejeon 34134, Republic of Korea

Corresponding author: Young-Dam Kim (e-mail: youngdamkim@cnu.ac.kr).

This work was supported by Samsung Research Funding Center of Samsung Electronics under Project Number SRFC-TB1803-51.

ABSTRACT This paper demonstrates the significance of employing the infinitesimal dipole modeling (IDM) in analyzing uniform circular array-orbital angular momentum (UCA-OAM) near-fields in terms of electromagnetic (EM) energy densities. The electric and magnetic field, and the EM energy densities of UCA-OAM waves are theoretically analyzed and numerically estimated where the spatial distribution of EM Lagrangian density and complex Helicity is visualized. It is validated that the IDM is more accurate than the conventional far-field assumption in evaluating the near-fields of UCA-OAM waves as the EM Lagrangian density and the complex Helicity are clearly depicted based on the IDM, while they are unobservable with the far-field assumption. The visualization of EM Lagrangian density and complex Helicity can be beneficial in designing UCA-OAM communication system as it suggests the mutual coupling between antennas by describing the regions of reactive EM energy densities and non-orthogonal EM fields in the near-field region.

INDEX TERMS Orbital Angular Momentum (OAM), Near-field Analysis, Infinitesimal Dipole Modeling (IDM), EM Lagrangian Density, Complex Helicity

I. INTRODUCTION

The concept of orbital angular momentum (OAM) has gained prominence as an intriguing property of light, attracting increasing attention from the academic community [1], [2]. OAM of light denotes the revolution of electric field around the beam axis where the light beam is given a spatial phase distribution of $il\phi$. Here, ϕ is the azimuthal angle along the beam axis and the integer mode number l indicates that azimuthal phase change in a cross section is $2\pi l$ for a revolution. In this way, light vortices having different mode numbers become spatially orthogonal to each other [3].

Allen *et al*. were the first to experimentally prove that light can carry OAM with Laguerre-Gaussian (LG) laser modes [4]. Later, it was found that radio waves and acoustic beams can also convey OAM [5]–[7]. The inherent orthogonality of OAM enables mode multiplexing, with the potential to significantly enhance channel capacity in communication. For this reason, the application of OAM has garnered attention as a promising technology for 6G communication [8] and it has been extensively explored in both optical [9]–[13] and radio wave communication fields [6], [14]–[20]. Besides, it has been discovered that OAM can be applied in astronomy [21], [22], imaging [23], [24], and rotational Doppler shift detection [25].

Generation of OAM radio waves has been investigated for varied physical structures such as spiral phase plate [15], [18]–[20], ring resonator [16], Cassegrain reflector [17], [26], reflectarrays [27], transmitarrays [28], metasurfaces [29], [30], and uniform circular array (UCA) [24], [31], [32]. Furthermore, the characteristics of OAM have been explored regarding various physical factors. The effect of optical loss and grating imperfection on the OAM mode purity was investigated [33]. The channel capacity of OAM channels was assessed based on paraxiality and orthogonality [34]. In [35], OAM-based multiple-input–multiple-output (MIMO) was found to provide larger channel capacity than the conventional MIMO for a transmission distance longer than a particular threshold. The influences of receiver aperture and the multipath on the power loss and the crosstalk of an OAM-multiplexed link were analyzed through simulation [36].

As mentioned above, UCA is one of the options for creating OAM waves. When a UCA has *N* array elements, OAM waves can be generated by feeding each *n*-th element

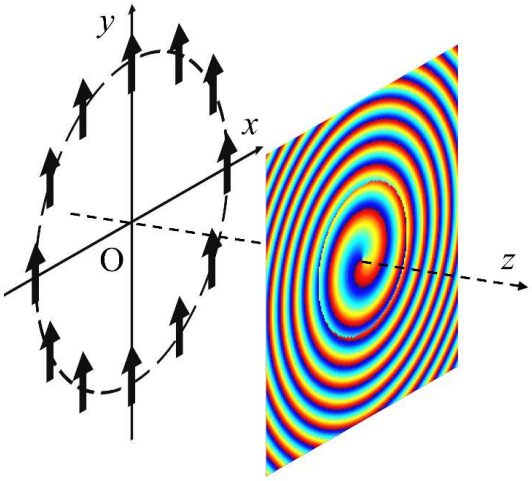

FIGURE 1. Phase distribution of OAM wave transmitted from UCA.

with an azimuthal phase of $-i2\pi ln/N$ for the mode number l. The OAM multiplexing based on UCA has been analyzed in multiple research works. In [37], the UCA-OAM wave was theoretically analyzed, revealing that the antenna array in the same direction demonstrated the highest energy transmission efficiency. Additionally, a theoretical analysis was conducted to assess the channel capacity of UCA-OAM and UCA-MIMO systems [38]. Beam steering of UCA-OAM waves was investigated in terms of mitigating performance degradation from misalignment [39] and maintaining high mode isolation during beam steering [40].

The transmission of UCA-OAM waves primarily occurs within the near-field region, because a UCA-OAM communication system has substantial dimensions and requires operation at a high frequency to achieve a high data transmission rate over long distances [41]–[43]. In addition, OAM-multiplexed transmission has the potential to be applied in a high-capacity backhaul link of 6G [2]. Therefore, the near-fields of UCA-OAM waves need to be accurately analyzed. However, conventional analysis of UCA-OAM waves is derived under the assumption that each array element of UCA radiates a far-field [24], [31], [37], making it inaccurate for the near-field analysis. Therefore, fields of UCA-OAM waves need to be rigorously analyzed without the far-field assumption.

Infinitesimal dipole modeling (IDM) is an accurate and efficient technique for describing the current distribution of an antenna [44]. By employing the IDM, the antenna current distribution is equivalently modeled as infinitesimal dipoles (IDs). IDs at fixed positions are extracted based on a known field simulation or measurement result of the antenna through an iterative optimization method such as the least-squares method (LSQR). Then, the near-field radiated from the antenna can be readily calculated by re-radiating electric fields from the extracted IDs [45]. Numerous studies have been conducted on the application of the IDM. The IDM was employed to improve the prediction of the wideband beam pattern of the antenna array [46]. The mutual admittance of two random antennas in nonplanar skew positions was estimated via the IDM [47]. The IDM also facilitates antenna diagnostics and characterization with limited measurement data [48], [49]. Additionally, the S21 between two antennas was directly estimated based on the IDM [50].

Electromagnetic (EM) Lagrangian density and complex Helicity are distinctive EM energy densities which can be observed in the near-field region of EM fields [51]–[53]. The EM Lagrangian density indicates the region where the electric and magnetic energy density are not balanced. The complex Helicity appears where the electric and magnetic field are not orthogonal to each other. Analyzing EM energy densities based on the IDM can prove valuable in the design of UCA-OAM communication systems by offering insights into mutual coupling between antennas. Visualization of the EM Lagrangian density and the Complex Helicity reveals the regions of the non-propagating(reactive) EM energy densities and non-orthogonal EM fields between transmitting and receiving UCA antennas or between transmitting UCA antennas with different radii sharing the same axis. For analyzing the EM energy densities, it is essential to achieve both electric and magnetic near-field, which is possible through the IDM. Nonetheless, in the literature, little effort has been made to analyze and utilize the magnetic field using the IDM.

This paper highlights the superiority of the IDM-based near-field analysis for UCA-OAM waves over the conventional far-field assumption. The array elements of the UCA are modeled as IDs where each element radiates exact fields without the far-field assumption. The electric and magnetic fields of UCA-OAM waves are both theoretically and numerically analyzed through the IDM, where the EM energy densities in near-field regions are also estimated. The near-fields and EM energy densities assessed based on the IDM are compared to those obtained with the far-field assumption and the results of commercial full-wave simulation based on the method of moments (MoM). The IDM-based analysis shows good agreement with the results achieved using MoM and it also demonstrates much better accuracy in assessing UCA-OAM near-field energy densities than the analysis via far-field assumption. In a recent publication [54], the near-fields of UCA-OAM waves were analyzed for various parameters using Hertzian dipoles. However, the analysis presented in this paper is distinguished from previous research by demonstrating the superiority of the IDM over the far-field assumption through visualization of near-fields and EM energy densities. Interestingly, the magnitude of normalized complex Helicity exhibits distinct spatial distributions according to the sign of the OAM mode.

In section II, the near-fields and EM energy densities of UCA-OAM waves are theoretically analyzed based on the conventional far-field assumption and the IDM. In Section III, UCA-OAM near-fields and EM energy densities are

numerically analyzed and the analysis results of the IDM are compared to those of the far-field assumption and the full-wave simulation results. Section IV presents the conclusion.

II. THEORETICAL ANALYSIS

A. THEORETICAL ANALYSIS BASED ON THE FAR-FIELD ASSUMPTION

In this section, UCA-OAM near-fields and EM energy densities are theoretically analyzed based on the conventional far-field assumption. We refer to [37] where N antenna arrays of the UCA are electrically short dipoles on the xy plane centered around the z axis. Additionally, it is assumed that there is no mutual coupling between antenna arrays. As shown in Figure 1, each dipole antenna is aligned in y axis direction. The OAM waves are produced by exciting each n-th element with a current $I_n = e^{-il\phi_n}$ for an integer mode number l where $\phi_n = 2\pi n / N$. Based on $e^{-i\omega t}$ convention where ω is the angular frequency, the magnetic vector potential at an observation point $\mathbf{r} = (r, \theta, \phi)$ produced by n-th array element at position $\mathbf{r}_n$ is described as

$$\mathbf{A}_n(\mathbf{r}) = \hat{y}\frac{d\mu_0}{4\pi} e^{-il\phi_n} \frac{e^{ik|\mathbf{r}-\mathbf{r}_n|}}{|\mathbf{r}-\mathbf{r}_n|} \tag{1}$$

where d is the length of each short dipole antenna, μ_0 is the permeability of free-space, k is the wavenumber, and $\hat{y}$ is unit y vector.

For $|\mathbf{r}| = r \gg a$ where a is the radius of the UCA, the far-field assumption can be applied. Then the distance from n-th element to the observation point is approximated as $|\mathbf{r}-\mathbf{r}_n| \approx r$ and the phase is approximated as $e^{ik|\mathbf{r}-\mathbf{r}_n|} \approx e^{ik(r-\hat{r}\cdot\mathbf{r}_n)}$, which can be described as $e^{ikr-ika\sin\theta\cos(\phi-\phi_n)}$ in this case. Then the magnetic vector potential at $\mathbf{r}$ is depicted as

$$\begin{aligned}\mathbf{A}(\mathbf{r}) &= \hat{y}\frac{\mu_0 d}{4\pi r} e^{ikr} \sum_{n=1}^{N} e^{-il\phi_n} e^{-ika\sin\theta\cos(\phi-\phi_n)} \\ &\approx \hat{y}\frac{\mu_0 d e^{i(kr-l\phi)}}{4\pi r} N(-i)^l J_l(ka\sin\theta) \\ &= \left(\hat{r}\sin\theta\sin\phi + \hat{\theta}\cos\theta\sin\phi + \hat{\phi}\cos\phi\right) \\ &\quad \frac{\mu_0 d e^{i(kr-l\phi)}}{4\pi r} N(-i)^l J_l(ka\sin\theta)\end{aligned} \tag{2}$$

where $J_l(ka\sin\theta)$ is the Bessel function and $\hat{r}$, $\hat{\theta}$, $\hat{\phi}$ are unit vectors of the spherical coordinate system. The electric field with the far-field assumption can be calculated as $\mathbf{E}(\mathbf{r}) = i\omega(\mathbf{A}_\theta + \mathbf{A}_\phi)$, which is denoted as

$$\begin{aligned}\mathbf{E}(\mathbf{r}) = &\frac{i\omega\mu_0 d e^{i(kr-l\phi)}}{4\pi r} N(-i)^l J_l(ka\sin\theta) \\ &\left(\hat{x}T_x + \hat{y}T_y + \hat{z}T_z\right)\end{aligned} \tag{3}$$

where $\hat{x}$, $\hat{y}$, and $\hat{z}$ are unit x, y, and z vector, respectively.

$$\begin{aligned}T_x &= -\sin^2\theta\cos\phi\sin\phi \\ T_y &= \cos^2\theta + \sin^2\theta\cos^2\phi \\ T_z &= -\cos\theta\sin\theta\sin\phi.\end{aligned} \tag{4}$$

Then the magnetic field $\mathbf{H}(\mathbf{r})$ can be easily derived as $\mathbf{H}(\mathbf{r}) = \hat{r}\times\mathbf{E}(\mathbf{r})/\eta$ where η is the impedance of free-space. Then the magnetic field at $\mathbf{r}$ is

$$\begin{aligned}\mathbf{H}(\mathbf{r}) = &\frac{ikde^{i(kr-l\phi)}}{4\pi r} N(-i)^l J_l(ka\sin\theta) \\ &\left(-\hat{x}\cos\theta + \hat{z}\sin\theta\cos\phi\right).\end{aligned} \tag{5}$$

The EM energy densities of UCA-OAM waves can be estimated using (3) and (5). First, the total EM energy density u is defined as $u = w_e + w_m$ where $w_e = \varepsilon_0\mathbf{E}\cdot\mathbf{E}^*/4$ and $w_m = \mu_0\mathbf{H}\cdot\mathbf{H}^*/4$ are the electric and magnetic energy density, respectively. u is then expressed as

$$\begin{aligned}u &= \frac{1}{4}\left(\varepsilon_0\mathbf{E}\cdot\mathbf{E}^* + \mu_0\mathbf{H}\cdot\mathbf{H}^*\right) \\ &= \frac{\mu}{2}\left[\frac{kNdJ_l(ka\sin\theta)}{4\pi r}\right]^2\left(1-\sin^2\theta\sin^2\phi\right)\end{aligned} \tag{6}$$

where ε_0 is the permittivity of free-space. Furthermore, the EM Lagrangian density $\mathcal{L}$ and the complex Helicity $\mathcal{H}_c$ can be calculated as follows [53]:

$$\mathcal{L} = w_e - w_m = \frac{1}{4}\left(\varepsilon_0\mathbf{E}\cdot\mathbf{E}^* - \mu_0\mathbf{H}\cdot\mathbf{H}^*\right) = 0 \tag{7}$$

$$\mathcal{H}_c = \frac{1}{2}\left(\mathbf{E}\cdot\mathbf{H}^*\right) = 0. \tag{8}$$

(7) and (8) show that the EM Lagrangian density and the complex Helicity cannot be observed with the far-field assumption. In addition, the complex Poynting vector

$$\mathbf{S}_c = \frac{1}{2}\left(\mathbf{E}\times\mathbf{H}^*\right) = \frac{k\omega\mu_0}{2r^2}\left[\frac{Nd}{4\pi}J_l(ka\sin\theta)\right]^2$$

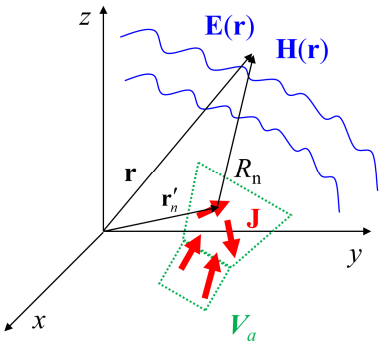

FIGURE 2. Arbitrary antenna expressed as a volume current density in volume V_a and electric field radiated by the antenna outside V_a.

$$\begin{bmatrix} T_y \sin\theta\cos\phi\,\hat{x} \\ -\left(T_z\cos\theta + T_x\sin\theta\cos\phi\right)\hat{y} \\ +T_y\cos\theta\,\hat{z} \end{bmatrix} \quad (9)$$

has a relation with u, $\mathcal{L}$, and $\mathcal{H}_c$ [53]:

$$\left|\mathcal{H}_c\right|^2 = c^2\left(u^2 - \mathcal{L}^2\right) - \left|\mathbf{S}_c\right|^2. \quad (10)$$

where c is the speed of light in free-space.

B. THEORETICAL ANALYSIS BASED ON THE IDM

In this section, we utilize the IDM to analyze the near-fields of the UCA-OAM waves. As described in Figure 2, an arbitrary antenna can be equivalently expressed as a volume current density $\mathbf{J}$ (A/m^2) in the volume $\boldsymbol{V}_a$ that contains the antenna in a linear, homogeneous, and isotropic medium. Then the electric field $\mathbf{E}$ (V/m) and magnetic field $\mathbf{H}$ (A/m) radiated from the antenna are expressed as

$$\mathbf{E}(\mathbf{r}) = \iiint_{V_a} \bar{\mathbf{G}}^E(\mathbf{r},\mathbf{r}')\,\mathbf{J}(\mathbf{r}')\,dv' \quad (11)$$

$$\mathbf{H}(\mathbf{r}) = \iiint_{V_a} \bar{\mathbf{G}}^H(\mathbf{r},\mathbf{r}')\,\mathbf{J}(\mathbf{r}')\,dv' \quad (12)$$

where $\mathbf{r}$ is the observation point outside $\boldsymbol{V}_a$ and $\mathbf{r}'$ is the position of the source inside $\boldsymbol{V}_a$. $\bar{\mathbf{G}}^E$ and $\bar{\mathbf{G}}^H$ are the dyadic Green's functions for electric field and magnetic field, respectively where they reflect the response of $\mathbf{J}$. Then the dyadic green's functions for $\mathbf{r} \neq \mathbf{r}'$ can be derived as [55]

$$\bar{\mathbf{G}}^E(\mathbf{r},\mathbf{r}') = i\omega\mu_0\left[\left(\bar{\mathbf{I}} + \frac{1}{k^2}\nabla\nabla^T\right)g(\mathbf{r},\mathbf{r}')\right] \quad (13)$$

$$\bar{\mathbf{G}}^H(\mathbf{r},\mathbf{r}') = \nabla g(\mathbf{r},\mathbf{r}')\times\bar{\mathbf{I}} \quad (14)$$

where $\nabla^T = \left[\partial/\partial x,\ \partial/\partial y,\ \partial/\partial z\right]$ is del-operator and the superscription T means transpose operator. In addition, $\bar{\mathbf{I}}$ is unit dyadic where $\bar{\mathbf{I}}\mathbf{A} = \mathbf{A}$ and the scalar free-space Green's function g is

$$g(\mathbf{r},\mathbf{r}') = \frac{e^{ik|\mathbf{r}-\mathbf{r}'|}}{4\pi|\mathbf{r}-\mathbf{r}'|}. \quad (15)$$

Here, the volume current density $\mathbf{J}$ in $\boldsymbol{V}_a$ can be alternatively expressed as electric IDs [45] as

$$\mathbf{J}(\mathbf{r}) = \sum_{n=1}^{N}\mathbf{p}_n\delta(\mathbf{r}-\mathbf{r}'_n) \quad (16)$$

where $\mathbf{p}_n$ describes n-th complex electric dipole moment vector. Then we can rewrite the radiated electric field and magnetic field by substituting (16) into (11) and (12), which can be expressed as

$$\mathbf{E}(\mathbf{r}) = \frac{i}{4\pi\omega\varepsilon_0}\sum_{n=1}^{N}\begin{bmatrix} k^2\left((\mathbf{n}_n\times\mathbf{p}_n)\times\mathbf{n}_n\right)\dfrac{e^{ikR_n}}{R_n} + \\ \left(3\mathbf{n}_n(\mathbf{n}_n\cdot\mathbf{p}_n) - \mathbf{p}_n\right)\left(\dfrac{-ik}{R_n} + \dfrac{1}{R_n^2}\right)\dfrac{e^{ikR_n}}{R_n} \end{bmatrix} \quad (17)$$

$$\mathbf{H}(\mathbf{r}) = \frac{1}{4\pi}\sum_{n=1}^{N}\left[(\mathbf{n}_n\times\mathbf{p}_n)\left(ik - \frac{1}{R_n}\right)\frac{e^{ikR_n}}{R_n}\right] \quad (18)$$

where $\mathbf{n}_n$ represents the unit vector from n-th ID at $\mathbf{r}_n'$ to the observation point $\mathbf{r}$ and R_n is $\left|\mathbf{r}-\mathbf{r}'_n\right|$.

For a UCA antenna shown in Fig. 1, we represent each antenna array as an ID. The position of n-th ID can be depicted as $\mathbf{r}'_n(x'_n, y'_n, z'_n) = \hat{x}a\cos\phi_n + \hat{y}a\sin\phi_n$ and n-th ID is denoted as $\mathbf{p}_n = e^{-il\phi_n}\hat{y}$ for mode l where $\phi_n = 2n\pi/N$ and $\hat{x}$ and $\hat{y}$ are unit x and y vector, respectively. Then the electric field and magnetic field of UCA-OAM waves can be represented as

$$\mathbf{E}(\mathbf{r}) = \frac{-i}{4\pi\omega\varepsilon_0}\sum_{n=1}^{N}\begin{bmatrix} \dfrac{w_n e^{-i(l\phi_n - kR_n)}}{R_n^5}\left(k^2R_n^2 + 3ikR_n - 3\right) \\ \begin{bmatrix} \hat{x}(x-x'_n)(y-y'_n) \\ +\hat{y}\left(\left((y-y'_n)^2 - \dfrac{R_n^2}{3}\right) + \dfrac{-2k^2R_n^4}{3k^2R_n^2 + 9ikR_n - 9}\right) \\ +\hat{z}(y-y'_n)z \end{bmatrix} \end{bmatrix} \quad (19)$$

$$\mathbf{H}(\mathbf{r}) = \frac{1}{4\pi}\sum_{n=1}^{N}\frac{w_n e^{-i(l\phi_n - kR_n)}}{R_n^2}\left(ik - \frac{1}{R_n}\right)\left[-\hat{x}z + \hat{z}(x-x'_n)\right]. \quad (20)$$

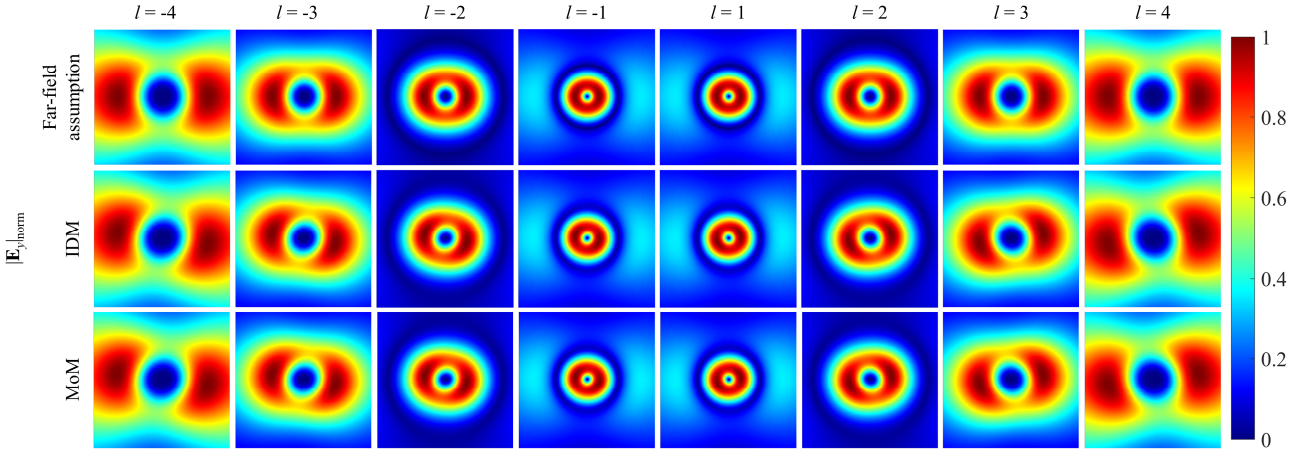

FIGURE 3. **Estimation results of the normalized magnitude of E_y.**

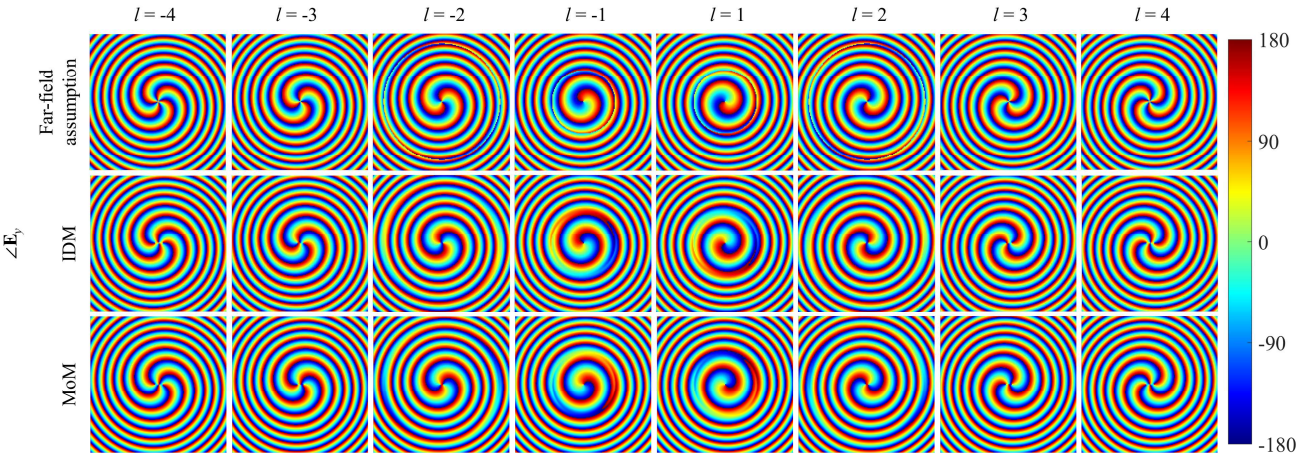

FIGURE 4. **Estimation results of the phase (deg) distribution of E_y.**

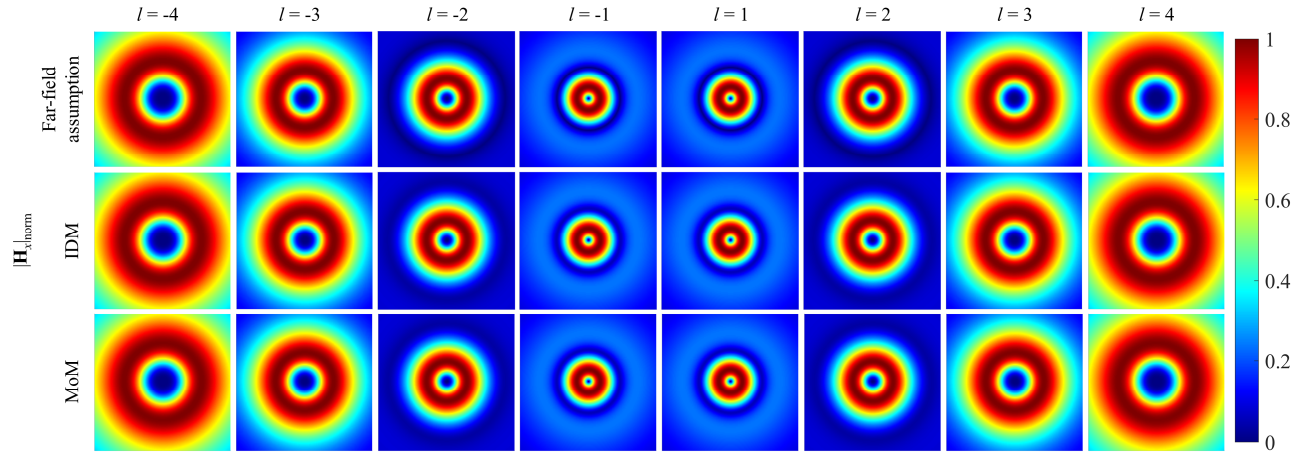

FIGURE 5. **Estimation results of the normalized magnitude of H_x.**

III. NUMERICAL ANALYSIS

In this section, electric field, magnetic field, and EM energy densities of UCA-OAM waves are numerically analyzed based on the equations acquired in the previous section. In addition, commercial MoM-based full-wave simulation is employed to verify the numerical analysis. The numerical analysis results estimated with the far-field assumption are compared to the results calculated based on the IDM and the MoM. For all three analysis methods, the radius of the UCA is λ and the dimensions of the observation plane were set as

This article has been accepted for publication in IEEE Access. This is the author's version which has not been fully edited and
content may change prior to final publication. Citation information: DOI 10.1109/ACCESS.2024.3412076

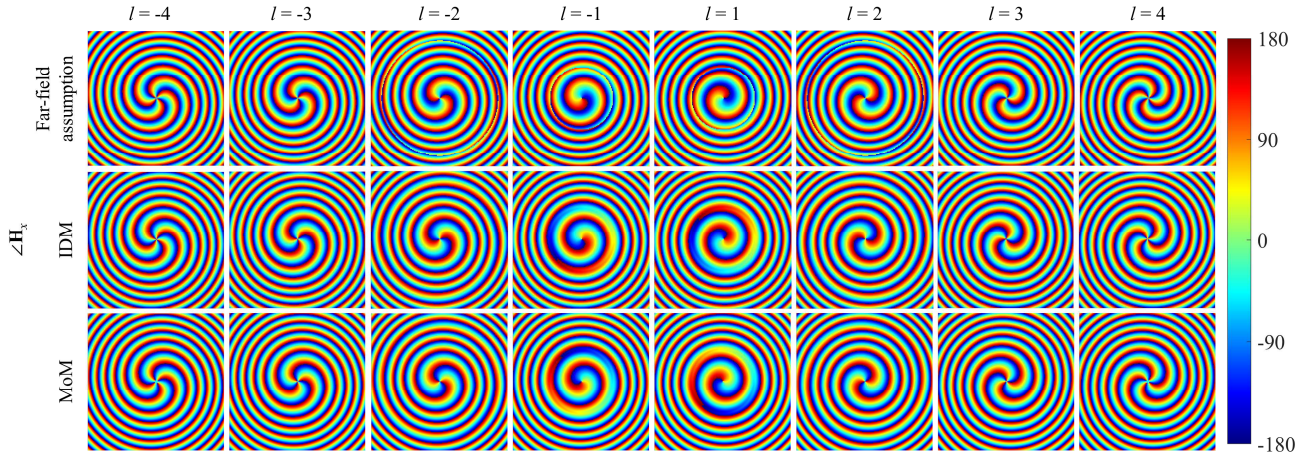

FIGURE 6. Estimation results of the phase (deg) distribution of H_x.

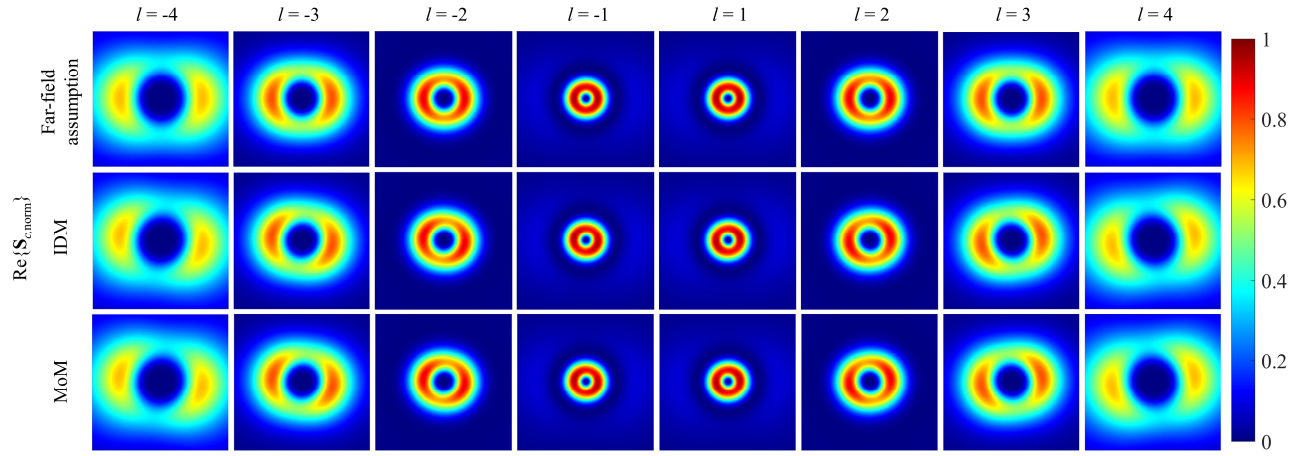

FIGURE 7. Estimation results of the real part of the normalized complex Poynting vector.

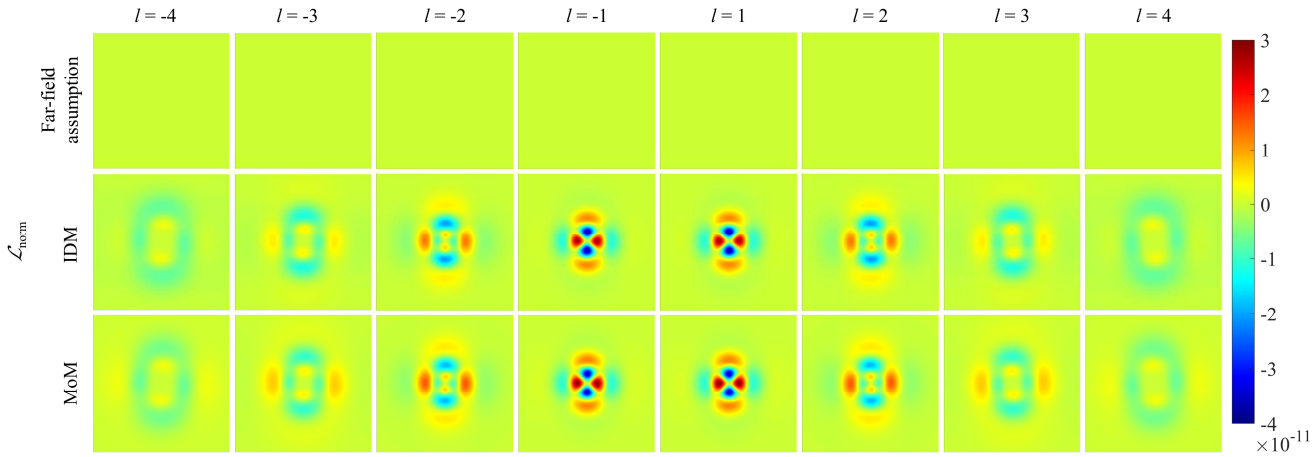

FIGURE 8. Estimation results of the EM Lagrangian density.

20λ in both x and y directions at $z = 6\lambda$ where its center coincides with the center of the UCA. Here, λ is the wavelength. The numerical analysis is done for frequency of 83.5 GHz. The number of array elements N for the far-field assumption and the IDM is 100, while the number of elements for the MoM simulation is set to 16 for calculation efficiency. The length of each short dipole for the far-field assumption and the MoM simulation is $\lambda/10$. First, y component of the electric field $\mathbf{E}_y$ and the x component of the magnetic field $\mathbf{H}_x$ are analyzed as they carry OAM of mode l with the highest energy efficiency [37], therefore the properties of OAM waves can be well observed. The analysis

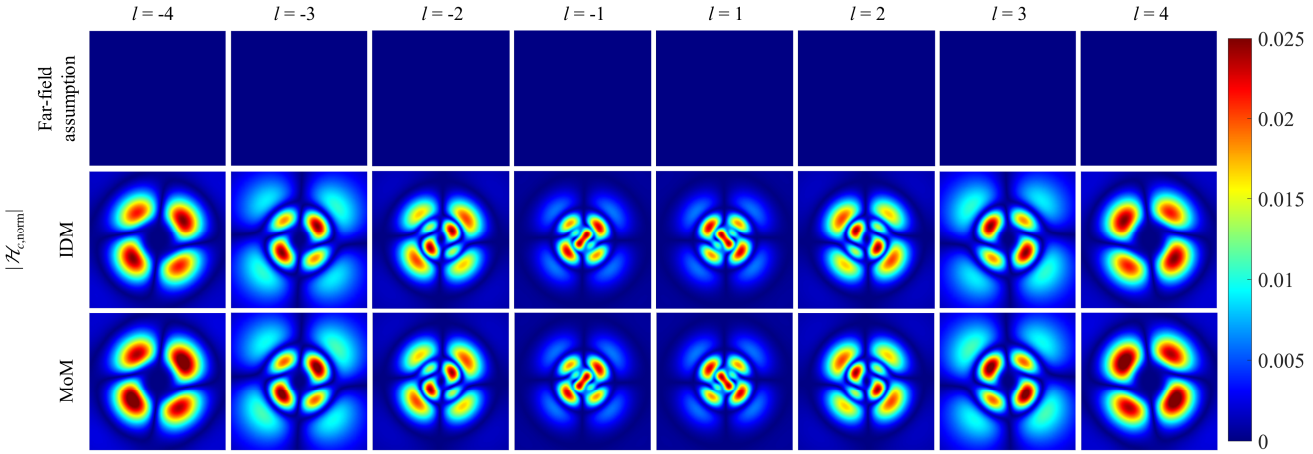

FIGURE 9. **Estimation results of the normalized magnitude of the Complex Helicity.**

is done for eight OAM modes: $l=-4$, $l=-3$, $l=-2$, $l=-1$, $l=1$, $l=2$, $l=3$, $l=4$.

Figure 3 and 4 show the normalized magnitude and phase distribution of $\mathbf{E}_y$ estimated based on the far-field assumption, the IDM, and the MoM. The normalized magnitude is acquired by dividing the magnitude by the maximum value on the observation plane. The donut-shaped vortex with amplitude null at the center and azimuthal phase change is observed for all three analysis methods. The far-field assumption results show good agreement with the IDM results except for slight rotations of the vortices in the magnitude of $\mathbf{E}_y$ in the IDM cases. These rotations are also observable in the MoM results. Besides, the OAM wave spreads more as the absolute value of the mode number increases. In Figure 5 and 6, the normalized magnitude and phase distribution of $\mathbf{H}_x$ are presented. The magnetic field also shows the vortex with clear azimuthal phase distribution and amplitude null at the center where the results of the far-field assumption match well with the IDM and the MoM.

Based on the estimated EM fields, EM energy densities of the UCA-OAM waves are analyzed. The real part of the normalized complex Poynting vector $\mathrm{Re}\{\mathbf{S}_{c,\mathrm{norm}}\}$, the normalized EM Lagrangian density $\mathcal{L}_{\mathrm{norm}}$, and the normalized magnitude of complex Helicity $|\mathcal{H}_{c,\mathrm{norm}}|$ are assessed. Each EM energy density value was normalized by $cu_{\max}$ where $u_{\max}$ is the maximum total EM energy density on the observation plane. In Figure 7, $\mathrm{Re}\{\mathbf{S}_{c,\mathrm{norm}}\}$ estimated with the far-field assumption matches well with the results of the IDM and the MoM although there is small difference in the shape of the vortices. In Figure 8 and 9, estimation results of $\mathcal{L}_{\mathrm{norm}}$ and $|\mathcal{H}_{c,\mathrm{norm}}|$ are depicted for three analysis methods. As shown in (7) and (8), the EM Lagrangian density and the complex Helicity are unobservable using the far-field assumption.

However, when employing the IDM, $\mathcal{L}_{\mathrm{norm}}$ and $|\mathcal{H}_{c,\mathrm{norm}}|$ become clearly discernible and the IDM results agree well with the MoM results. Since our proposed method is based on rigorous formulas that are applicable regardless of frequency, it operates effectively even at higher frequencies. This validates that the UCA-OAM near-fields can be analyzed more accurately based on the IDM than with the conventional far-field assumption. Furthermore, numerical analysis can be much more efficiently conducted through the IDM while still maintaining accuracy compared to full-wave simulations. The EM Lagrangian density visualizes the regions of unbalanced electric and magnetic energy density, while the complex Helicity indicates where the electric field and magnetic field are not orthogonal. In addition, the sign of the OAM mode is distinguishable by assessing the complex Helicity. The regions of relatively high $|\mathcal{H}_{c,\mathrm{norm}}|$ can lie on a straight line, where the OAM mode is positive for the line with a negative slope and the mode is negative for the line with a positive slope.

IV. CONCLUSION

In this paper, we demonstrate the significance of utilizing the IDM in analyzing the UCA-OAM near-fields by estimating the distribution of the normalized EM Lagrangian density $\mathcal{L}_{\mathrm{norm}}$ and the normalized magnitude of complex Helicity $|\mathcal{H}_{c,\mathrm{norm}}|$ in the near-field region. The electric and magnetic field, and EM energy densities are theoretically analyzed based on the conventional far-field assumption and the IDM. The results of the theoretical analysis are numerically estimated to visualize the EM near-fields and EM energy densities. MoM-based full-wave simulation was also conducted to verify the accuracy of the IDM. It is demonstrated that the IDM is superior than the conventional method for analyzing the UCA-OAM near-fields as $\mathcal{L}_{\mathrm{norm}}$ and $|\mathcal{H}_{c,\mathrm{norm}}|$ are clearly observable based on the IDM, where they are imperceptible through the far-field assumption. The EM Lagrangian density denotes the areas of unbalanced electric and magnetic energy densities where the complex

Helicity indicates the spatial distribution of non-TEM fields. Therefore, estimating the EM Lagrangian density and the complex Helicity of UCA-OAM waves can be helpful in designing a UCA-OAM communication system as they are able to picture the mutual coupling between transmitting and receiving UCA antennas or mutual coupling between transmitting UCA antennas with different radii sharing the same axis.

For future work, the IDM technique can be used to model antennas that generate OAM propagation in reverse. This means that it is possible to reconstruct the equivalent sources of an actually measured OAM-generating antenna and analyze the EM energy density of the actual antenna. Moreover, the mutual coupling between UCA-OAM antennas will be studied by estimating EM energy densities and calculating S_{21} between UCAs using the IDM.

REFERENCES

[1] L. A. Rusch, M. Rad, K. Allahverdyan, I. Fazal, and E. Bernier, “Carrying data on the orbital angular momentum of light,” *IEEE Commun. Mag.*, vol. 56, no. 2, pp. 219–224, Feb. 2018.

[2] C. Zhang and Y. Wang, "Orbital angular momentum: new physical resource and dimension for future MIMO," *IEEE Commun. Mag.*, vol. 61, no. 10, pp. 148-154, Oct. 2023.

[3] A. E. Willner et al., “Optical communications using orbital angular momentum beams,” *Adv. Opt. Photon.*, vol. 7, no. 1, pp. 66-106, Mar. 2015.

[4] L. Allen et al., “Orbital angular momentum of light and the transformation of Laguerre-Gaussian laser modes,” *Physical Rev. A*, vol. 45, no. 11, pp. 8185, Jun. 1992.

[5] B. Thidé et al., "Utilization of photon orbital angular momentum in the low-frequency radio domain,” *Phys. Rev. Lett.*, vol. 99, no. 8, pp. 087701, Aug. 2007.

[6] F. Tamburini et al, Encoding many channels on the same frequency through radio vorticity: First experimental test, *New J. Phys.*, vol. 14 no.3, pp. 033001-1–033001-18, Mar. 2012.

[7] C. E. M. Démoré, Z. Yang, A. Volovick, S. Cochran, M. P. MacDonald and G. C. Spalding, "Mechanical evidence of the orbital angular momentum to energy ratio of vortex beams,” *Phys. Rev. Lett.*, vol. 108, no. 19, pp.194301, May 2012.

[8] “Next G Alliance report: roadmap to 6G,” Next G Alliance, North America, Feb. 2022, Accessed: Nov. 5, 2023; [Online]. Available: https://www.nextgalliance.org/6g-library/

[9] G. Gibson et al., “Free-space information transfer using light beams carrying orbital angular momentum,” *Opt. Exp.*, vol. 12, no. 22, pp. 54485456, Nov. 2004.

[10] J. Wang et al., “Terabit free-space data transmission employing orbital angular momentum multiplexing,” *Nature Photon.*, vol. 6, pp. 488496, Jun. 2012.

[11] N. Bozinovic et al., “Terabit-scale orbital angular momentum mode division multiplexing in fibers,” *Sci.*, vol. 340.6140, pp. 1545-1548, June, 2013.

[12] R. M. Nejad et al., “Mode division multiplexing using orbital angular momentum modes over 1.4-km ring core fiber,” *J. Lightw. Technol.*, vol. 34, pp. 4252-4258, Jul. 2016.

[13] J. Wang, S. Chen, and J. Liu, “Orbital angular momentum communications based on standard multi-mode fiber,” *APL Photon.*, vol. 6, no. 6, 2021, Art. no. 060804.

[14] F. E. Mahmouli and S. D. Walker, "4-Gbps uncompressed video transmission over a 60-GHz orbital angular momentum wireless channel,” *IEEE Wireless Commun. Lett.*, vol. 2, no. 2, pp. 223-226, Apr. 2013.

[15] Y. Yan et al., “High-capacity millimetre-wave communications with orbital angular momentum multiplexing,” *Nature Commun.*, vol. 5, no. 1, pp. 4876, Dec. 2014.

[16] X. Hui et al., “Multiplexed millimeter wave communication with dual orbital angular momentum (OAM) mode antennas,” *Sci. Rep.*, vol. 5, pp. 10148, May 2015.

[17] W. Zhang et al., “Mode division multiplexing communication using microwave orbital angular momentum: An experimental study,” *IEEE Trans. Wireless Commun.*, vol. 16, no. 2, pp. 1308–1318, Feb. 2017.

[18] Y. Ren et al., "Line-of-sight millimeter-wave communications using orbital angular momentum multiplexing combined with conventional spatial Multiplexing," *IEEE Trans. Wireless Commun.*, vol. 16, no. 5, pp. 3151-3161, May 2017.

[19] H. Zhou et al., “Experimental demonstration of 8-Gbit/s QPSK communications using two multiplexed orbital-angular-momentum beams in the 0.27–0.33 THz range,” *in Proc. Conf. Lasers Electro-Opt. (CLEO)*, May 2021, pp. 1–2.

[20] H. Zhou et al., “Utilizing multiplexing of structured THz beams carrying orbital-angular-momentum for high-capacity communications,” *Opt. Exp.*, vol. 30, no. 14, pp. 25418–25432, 2022.

[21] N. M. Elias II., “Photon orbital angular momentum in astronomy,” *Astron. Astrophys.*, vol. 492, pp. 883–922, Oct. 2008.

[22] M. Harwit, “Photon orbital angular momentum in astrophysics," *The Astrophysical J.*, vol. 597, no. 2, pp. 1266-1270, Nov. 2010.

[23] C.A. Fitzpatrick et al., “High-capacity imaging and rotationally insensitive object identification with correlated orbital angular momentum states,” *Int. J. Quantum Inform.*, vol. 12, no. 7/8, pp. 1560013, Dec. 2014.

[24] K. Liu et al., “Orbital-angular momentum-based electromagnetic vortex imaging,” *IEEE Antennas Wireless Propag. Lett.*, vol. 14, pp. 711–714, 2015.

[25] M. P. Lavery et al, "Detection of a spinning object using light’s orbital angular momentum," *Sci.*, vol. 341, no. 6145, pp. 537-540, Aug. 2013.

[26] W.J. Byun et al., “Simple generation of orbital angular momentum modes with azimuthally deformed cassegrain subreflector,” *IET Electron. Lett.*, vol. 51, no. 19, pp. 1480–1482, Sep. 2015.

[27] W. J. Byun, H. Do Choi, and Y. H. Cho, “Orbital angular momentum (OAM) antennas via mode combining and canceling in near-field,” *Sci. Rep.*, vol. 7, no. 1, pp. 1–9, Oct. 2017

[28] A. V. Shahmirzadi and A. A. Kishk, "OAM carrying vortex beam mode interconversion using modular cascaded transmitarrays," *IEEE Trans. Microw. Theory Techn.*, vol. 70, no. 7, pp. 3591-3605, July 2022.

[29] H. Chung, D. Kim, E. Choi, and J. Lee, “E-band metasurface-based orbital angular momentum multiplexing and demultiplexing,” *Laser Photon. Rev.*, vol. 16, no. 6, 2022, Art. no. 2100456.

[30] Z. Xie et al., "Phase off-axis modulation metasurface for orbital angular momentum mode multiplexing/demultiplexing," *J. Lightw. Technol.*, vol. 41, no. 2, pp. 540-546, Jan., 2023.

[31] S. M. Mohammadi et al., “Orbital angular momentum in radio—A system study,” *IEEE Trans. Antennas Propag.*, vol. 58, no. 2, pp. 565–572, Feb. 2010.

[32] M. I. W. Khan, "A 0.31-THz orbital-angular-momentum (OAM) wave transceiver in CMOS with bits-to-OAM mode mapping," *IEEE J. Solid-State Circuits*, vol. 57, no. 5, pp. 1344-1357, May 2022.

[33] C. Sun et al., "Analysis of OAM mode purity of integrated optical vortex beam emitters," *IEEE Photon. J.*, vol. 9, no. 1, pp. 1-7, Feb. 2017.

[34] A. Sawant et al., “Ultimate capacity analysis of orbital angular momentum channels,” *IEEE Wireless Commun.*, vol. 28, no. 1, pp. 90–96, 2021.

[35] L. Wang, X. Ge, R. Zi and C. -X. Wang, "Capacity analysis of orbital angular momentum wireless channels," *IEEE Access*, vol. 5, pp. 23069-23077, Oct. 2017.

[36] X. Su et al., "Receiver aperture and multipath effects on power loss and modal crosstalk in a THz wireless link using orbital-angular-momentum multiplexing,” *Sci. Rep.*, vol. 12, no. 1, Aug. 2022, Art. no. 14053.

[37] D. Liu et al., "Theoretical analysis and comparison of OAM waves generated by three kinds of antenna array,” *Digit. Commun. Netw.*, vol. 7, no. 1, pp. 16-28, 2021.

[38] G.-T. Gil, J. Y. Lee, H. Kim and D.-H. Cho, "Comparison of UCA-OAM and UCA-MIMO systems for sub-THz band line-of-sight

spatial multiplexing transmission," *J. Commun. Netw.*, vol. 23, no. 2, pp. 83-90, Apr. 2021.

[39] R. Chen, H. Xu, M. Moretti and J. Li, "Beam steering for the misalignment in UCA-based OAM communication systems," *IEEE Wireless Commun. Lett.*, vol. 7, no. 4, pp. 582-585, Aug. 2018.

[40] W. Yu, B. Zhou, Z. Bu and Y. Zhao, "UCA based OAM beam steering with high mode isolation," *IEEE Wireless Commun. Lett.*, vol. 11, no. 5, pp. 977-981, May 2022.

[41] NEC. "NEC successfully demonstrates real-time digital OAM mode multiplexing transmission over 100 m in the 150 GHz-band for the first time.", NEC. Accessed: Nov. 5, 2023. [Online]. Available: https://www.nec.com/en/press/202003/global_20200310_01.html

[42] Y. Yagi, H. Sasaki, T. Yamada, and D. Lee, "200 Gb/s wireless transmission using dual-polarized OAM-MIMO multiplexing with uniform circular array on 28 GHz band," *IEEE Antennas Wireless Propag. Lett.*, vol. 20, no. 5, pp. 833–837, May 2021.

[43] Y. Yagi, H. Sasaki and D. Lee, "Prototyping of 40 GHz band orbital angular momentum multiplexing system and evaluation of field wireless transmission experiments," *IEEE Access*, vol. 10, pp. 130040-130047, 2022.

[44] M. Mikki and A. A. Kishk, "Theory and applications of infinitesimal dipole models for computational electromagnetics," *IEEE Trans. Antennas Propag.*, vol. 54, no. 5, pp. 1325–1337, May 2007.

[45] S. J. Yang and Y. D. Kim, "An accurate near-field focusing of array antenna based on near-field active element pattern and infinitesimal dipole modeling," *IEEE Access*, vol. 9, pp. 143771-143781, 2021.

[46] Y.-D. Kim, S.-J. Yang, N.-H. Myung and J. Yu, "Improved prediction of the wideband beam pattern shape of antenna array based on infinitesimal dipole modeling," *IEEE Antennas Wireless Propag. Lett.*, vol. 17, no. 12, pp. 2309-2313, Dec. 2018.

[47] Y.-D. Kim, S.-J. Yang, Y.-S. Kang, I.-J. Hwang and J.-W. Yu, "Mutual admittance of two arbitrary antennas in nonplanar skew positions based on infinitesimal dipole modeling," *IEEE Trans. Antennas Propag.*, vol. 67, no. 11, pp. 6705-6713, Nov. 2019.

[48] J.-I. Oh, S. J. Yang, S. Kim, J.-W. Yu and Y. D. Kim, "Antenna diagnostics based on infinitesimal dipole modeling with limited measurement on antenna aperture," *IEEE Antennas Wireless Propag. Lett.*, vol. 21, no. 5, pp. 923-927, May 2022.

[49] J.-H. Han, W. Lee and Y. D. Kim, "Infinitesimal dipole modeling from sparse far-field patterns for predicting electromagnetic characteristics of unknown antennas," *IEEE Trans. Antennas Propag.*, vol. 70, no. 11, pp. 10245-10252, Nov. 2022.

[50] D.-J. Yun, H. Kang, I.-J. Hwang and Y.-D. Kim, "Direct S_{21} calculation using infinitesimal dipole modeling," *IEEE Access*, vol. 11, pp. 118907-118915, 2023.

[51] D. Sarkar and Y. Antar, "Distribution of reactive energy density around antennas in time-harmonic regime: an electromagnetic Lagrangian approach," 2023, *TechRxiv*, doi: 10.36227/techrxiv.21654857.v3

[52] D. Sarkar and Y. Antar, "FDTD computation of space/time integrated electromagnetic Lagrangian: New insights into design of mutually coupled antennas," *IEEE J. Multiscale Multiphys. Comput. Tech.*, vol. 7, pp. 16–22, Feb. 2022.

[53] D. Sarkar and Y. M. M. Antar, "Antenna mutual coupling in near-field: insights using EM Lagrangian density and complex Helicity," *IEEE Antennas Wireless Propag. Lett.*, vol. 22, no. 11, pp. 2670-2674, Nov. 2023.

[54] A. Ž. Ilić et al., "Near-field formation of the UCA-based OAM EM fields and short-range EM power flux profiles," *J. Phys. A: Math. Theor.*, vol. 56, pp. 255701, May 2023.

[55] C.-T. Tai, *Dyadic Green Functions in Electromagnetic Theory*, Piscataway, NJ, USA:IEEE Press, 1994.

Jaehoon Jeong was born in Daegu, South Korea, in 1994. He received the B.S. degree in electrical engineering from the Ulsan National Institute of Science and Techology (UNIST), Ulsan, South Korea, in 2017. He worked as a Research Officer of National Defense at the Agency for Defense Development (ADD), Daejeon, South Korea from 2018 to 2021. He is currently an Engineer with the Korea Aerospace Research Insitute (KARI). He is also currently pursuing the M.S. degree with department of electronics, radio sciences & engineering and information communications engineering of Chungnam National University (CNU), Daejeon, South Korea. His current research interests include the analysis of electromagnetic waves and source reconstruction based on computational electromagnetics.

Young Dam Kim was born in Suwon, Korea, in 1988. He received the B.S. degree in electronics engineering from the Ajou University, Suwon, Korea, in 2011, and the M.S. and Ph. D. degree in electrical engineering from the Korea Advanced Institute of Science and Technology (KAIST), Daejeon, Korea, in 2013 and 2017, respectively. He worked as a senior engineer at the Samsung Electronics Network Business, Suwon, Korea, in 2017. He worked as a postdoc at the KAIST in 2018. He worked as a senior researcher in Agency for Defense Development (ADD) in Korea from 2019 to 2020. He is currently an assistant professor with the department of electronics engineering of Chungnam National University (CNU), Daejeon, Korea. His current research interests include the analysis of active phased antenna array and electromagnetic scattering problems based on applied computational electromagnetics.